

CHALMERS
UNIVERSITY OF TECHNOLOGY

Single-Shot Polarization Imaging of Vectorial Metasurfaces Using Cross-Grating Wavefront Microscopy

Downloaded from: https://research.chalmers.se, 2026-11-24 10:05 UTC

Citation for the original published paper (version of record):
Flamant, J., Marthy, B., Zangeneh Kamali, K. et al (2026). Single-Shot Polarization Imaging of Vectorial Metasurfaces Using Cross-Grating Wavefront Microscopy. ACS Nano, 20(42): 28193-28206. http://dx.doi.org/10.1021/acsnano.6c06635

N.B. When citing this work, cite the original published paper.

research.chalmers.se offers the possibility of retrieving research publications produced at Chalmers University of Technology. It covers all kind of research output: articles, dissertations, conference papers, reports etc. since 2004. research.chalmers.se is administrated and maintained by Chalmers Library

(article starts on next page)

ACS NANO

www.acsnano.org

Open Access

This article is licensed under CC-BY-NC-ND 4.0

Single-Shot Polarization Imaging of Vectorial Metasurfaces Using Cross-Grating Wavefront Microscopy

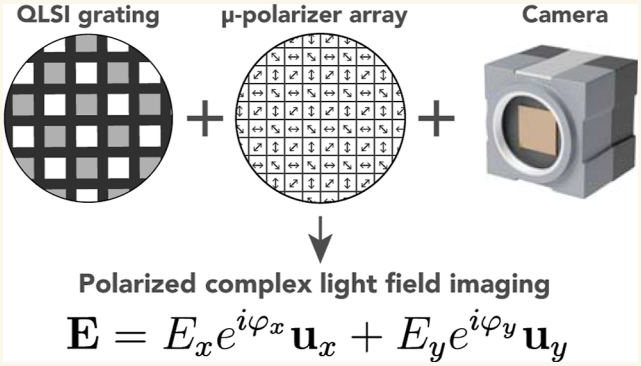
Julien Flamant, Baptiste Marthy, Khosro Zangeneh Kamali, Nathan Ullberg, Guillaume Demesy, Patrick Ferrand, Mikael Käll, and Guillaume Baffou*

Cite This: *ACS Nano* 2026, 20, 28193−28206

Read Online

ACCESS | Metrics & More | Article Recommendations | Supporting Information

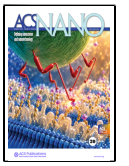
ABSTRACT: **Nanophotonics and optical microscopy are now tightly intertwined in modern research, as high-resolution optical characterization is essential for studying nanomaterials, such as dielectric and plasmonic nanoparticles, metasurfaces, and 2D materials. Yet, existing microscopy techniques are often complex to implement or limited to measuring light intensity, overlooking spectral, phase, and polarization features. Here, we report an optical microscopy approach capable of retrieving the full complex vectorial electromagnetic field at the image plane (that is, intensity, phase, and polarization of light) in a single acquisition. The method combines a polarization-sensitive camera with a two-dimensional diffraction grating (cross-grating) placed in close proximity to the image sensor. Beyond light beam characterization, we show how this configuration enables sample characterization in two image acquisitions, through Jones matrix imaging, from which we derive the complex transmittance tensor of metasurfaces. This accessible technique, easy to implement in any preexisting microscope, offers a comprehensive metrology platform for advanced studies of metasurfaces and 2D materials, in line with the growing interest in polarization-resolved nanophotonics.**



KEYWORDS: *polarimetry, microscopy, metasurfaces, cross-grating, wavefront imaging*

Light carries a wealth of information encoded not only in its intensity, but also in its phase, vectorial nature, and spectral content. This richness has driven the development of advanced imaging techniques capable of mapping more than intensity alone. In particular, over the past decade, polarimetric imaging techniques have experienced rapid growth, including Stokes,[1−4] full-Stokes[5−16] and Jones vector imaging.[6−8,10−15,17−29] Beyond the full characterization of a vectorial light beam, the ultimate goal of such techniques is often to retrieve the intrinsic polarization properties of the object with which the beam has interacted, for instance in the form of Jones or Mueller matrices.[6−8,10−31] Polarimetric imaging is straightforward when multiple acquisitions are permitted, for example by rotating polarizers or waveplates placed before and after the sample.[12,17,22,24,32−35] However, it becomes significantly more challenging when mechanical motion must be avoided and single-shot operation is required, as in the study of dynamic processes or vibration-sensitive systems. For this reason, a central challenge since the early 2000s has been to achieve single-shot polarimetric imaging.[5−8,10−16,18−21,23−26,28−30] Several strategies have therefore been proposed to address this challenge: Rather than distributing the measurements across time, the information can be (i) spatially divided at the image plane: the beam is split over different regions of the camera, each corresponding to a distinct polarization state (division of amplitude, DoAm);[10,20,24] (ii) divided at the pupil plane: the aperture stop of the imaging system is segmented into zones, each dedicated to a different polarization state (division of aperture, DoAp),[5−8,10−15,17−26,28,29] (iii) sampled directly at the detector using a micropolarizer array patterned onto the sensor surface, typically arranged in 2 × 2 superpixels measuring 0°, 45°, 90°, and 135° (division of focal plane, DoFP),[6,7,11−13,23,28−30] (iv) multiplexed interferometrically: all

Received: April 8, 2026
Revised: October 5, 2026
Accepted: October 6, 2026
Published: October 15, 2026



ACS Publications

© 2026 The Authors. Published by American Chemical Society

Downloaded from pubs.acs.org/ancac3/article-pdf/20/42/28193/6887767/2/acsnano.6c06635.pdf by guest on 06 November 2026

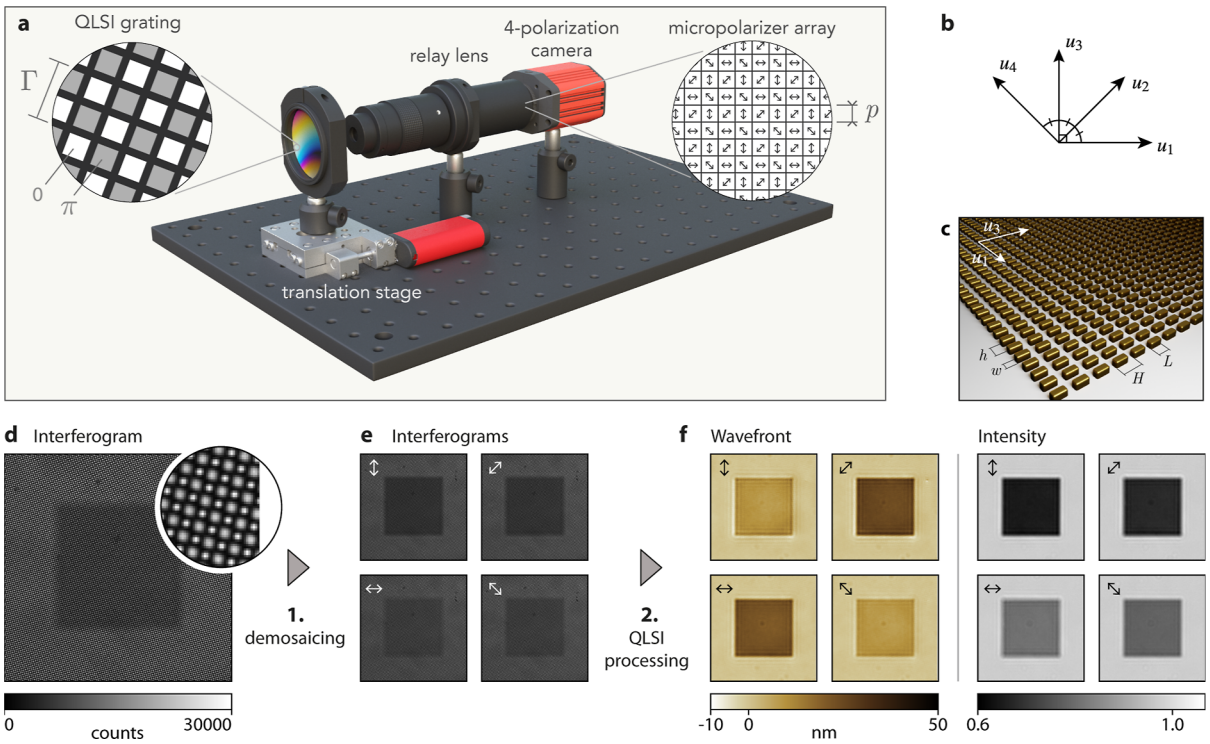


Figure 1. (a) Schematic of the polar-QLSI system, composed of 4 elements, namely a 2D (QLSI) grating, a relay lens, a micropolarizer array, and a CMOS camera. (b) Definition of the 4-axis system. (c) 3D representation of the gold nanorod sample. The nanorods are oriented vertically (along u_3) in the images. (d) Raw image captured by the camera, called the interferogram. (e) 4 subinterferograms, obtained by demosaicing of the raw image (d). (f) 4 wavefront and intensity images obtained from the 4 subinterferograms (e) using a QLSI algorithm.

polarization information is encoded into a single interferogram or fringe pattern at the image plane (division of channeled imaging, DoCI).[16]

In recent years, metasurfaces have been exploited in the implementation of several of these approaches.[7,10−12,14−16,28,36,37] However, metasurfaces typically require the use of a specific wavelength for which they were designed, thus limiting spectral investigations. Quantitative phase imaging (QPI) techniques have also been widely used in polarization imaging, mostly using digital holographic microscopy (DHM).[5,17,19−21,24−26,29,30,38] However, DHM requires a specific microscope and laser illumination. First, laser illumination makes any spectral study difficult. Then, it creates speckle noise and interference fringes on the image. Speckle noise is static, and cannot be diminished by averaging successive images.[39]

Currently, there is no polarimetric imaging technique that combines the advantages of single-shot operation, low noise, broadband, and simplicity.

In this article, we report an optical imaging technique capable of mapping the full vectorial electromagnetic field (both full-Stokes and Jones vector imaging) of a paraxial beam in a single acquisition. The technique leverages the association of a polarization camera and a 2-dimensional diffraction grating separated by a millimeter distance. We illustrate the potential of this technique in microscopy and focus on applications in nanophotonics by characterizing vectorial metasurfaces.[40] In addition to vectorial field characterization at the image plane (Jones vector imaging), the technique also retrieves the full tensorial optical properties of the imaged object (Jones matrix imaging). This technique, which we call polarization-resolved cross-grating wavefront microscopy (polar-CGM), combines the advantages of simplicity (as a camera-like add-on to any microscope), broadband, high signal-to-noise ratio, and single-shot operation.

RESULTS/DISCUSSION

Beyond the Scalar Approximation

Quantitative phase imaging (QPI) and wavefront imaging (WI) techniques[39,41−43] have marked a significant step forward by revealing information beyond intensity, namely the phase of light, thus providing access to the complex electric field amplitude of a light wave

$$\underline{E}(x, y) = |\underline{E}(x, y)|e^{i2\pi/\lambda W(x,y)} = |\underline{E}(x, y)|e^{i\phi(x,y)} \quad (1)$$

where W is the wavefront profile, ϕ the phase, and λ the wavelength. We use the optical convention $E(t) = \mathrm{Re}(\underline{E}e^{-i\omega t})$. In the following, we omit the underline used to denote complex quantities. Here, x and y denote the coordinates in the camera sensor plane. Imaging the phase of light has led to numerous applications since the early 2000s in biology[42−45] and nanophotonics.[38,46−49]

However, the mathematical description above assumes a scalar approximation of the light wave. In the most general case, a light wave is a vectorial field $\mathbf{E} = (E_x, E_y, E_z)$, and each component E_j is associated with a given intensity $I_j = |E_j|^2$ and a given phase $\phi_j = \arg(E_j)$. In many situations, including optical microscopy, the field is captured by a camera at a near-normal incidence, making E_z negligible. Under this so-called paraxial approximation, the field of interest is therefore

$$\mathbf{E}(x, y) = \sqrt{I_x(x, y)}\, e^{i\phi_x(x,y)}\mathbf{u}_x + \sqrt{I_y(x, y)}\, e^{i\phi_y(x,y)}\mathbf{u}_y \quad (2)$$

https://doi.org/10.1021/acsnano.6c06635
ACS Nano 2026, 20, 28193−28206

Downloaded from pubs.acs.org/ancac3/article-pdf/20/42/28193/6887767/2/acsnano.6c06635.pdf by guest on 06 November 2026

where $\mathbf{u}_x$ and $\mathbf{u}_y$ denote the canonical basis vectors in the $x - y$ plane. Consequently, full measurement of the electromagnetic field $\mathbf{E}(x, y)$ requires determining four scalar fields, namely I_x, I_y, ϕ_x, and ϕ_y.

Experimental Setup

Equation 2 highlights why imaging the optical phase is essential in polarimetric imaging. Digital holographic microscopy (DHM) has been the primary QPI technique used in this context.[5] However, DHM complicates spectral studies and leads to detrimental speckle noise that is difficult to suppress. In this study, we instead employ quadriwave lateral shearing interferometry (QLSI), a broadband WI technique that has already demonstrated strong performance in the investigation of nanomaterials[50−52] owing to its high signal-to-noise ratio and its compatibility with incoherent light sources, which facilitates broadband spectral measurements.

QLSI is based on the association of a camera and a special 2-dimensional (2D) diffraction grating separated by a millimeter distance, as sketched in Figure 1a.[53−56] In this study, instead of attaching the cross-grating to the camera, we used a relay lens to reimage the grating in front of the camera (Figure 1a).[46,57] This configuration enables fine adjustment of the grating/camera distance to optimize sensitivity,[58] and avoids the delicate removal of the hermetically sealed optical window of the camera sensor with the risk of damaging the sensor. This cross-grating, historically called a modified Hartmann mask (MHM), produces a dense array of bright spots on the camera. The related acquired image, called the interferogram, is processed to extract both the intensity and the wavefront (or equivalently the phase) profiles of a light beam. When a QLSI system is mounted on the output port of a microscope, the resulting method is called cross-grating wavefront microscopy (CGM).

To date, QLSI has been used only with regular CCD or CMOS cameras to image light fields in the scalar approximation. Here, we combine a custom-built QLSI system with a polarization camera, which comprises an array of linear micropolarizers, oriented along 4 directions at 0°, 45°, 90° and 135°, tiled in a 2 × 2 pattern (Figure 1a). Each micropolarizer is placed in front of one camera dexel (that is, a detector element, just like a pixel is a picture element). After a demosaicing step (Figure S1), this camera can deliver a set of 4 interferograms corresponding to 4 different light polarizations, 0, 45, 90, and 135°. We checked that the demosaicing step does not affect the quality and accuracy of the wavefront reconstruction (Section S5). We implement this custom-built polarization-resolved QLSI device in a microscope and call the related technique polar-CGM.

Polar-CGM measurements lead to a reduction in image definition (i.e., number of pixels). If one wants to encode information beyond intensity in a single image acquired in a single shot, the price to pay is necessarily a reduction in spatial resolution, regardless of the approach used (CGM, DHM or any single-shot QPI). Techniques that preserve the full sensor resolution in the reconstructed images necessarily rely on multiple acquisitions. In polar-CGM, an area of 6 × 6 intensity pixels of the interferogram produces one pixel of intensity + phase + polarization in the final polar-CGM images. This reduction in image definition is the price to pay to gain more information than only the intensity, but does not necessarily mean a reduction in image resolution (see discussion in Supporting Information, Section S2).

In microscopy, the actual intensity and wavefront/phase images impinging on the camera sensor are usually not what is measured in QPI. Such quantities are strongly affected by the inherent imperfections of microscopes (aberrations and dust particles), in particular the wavefront/phase image (see Supporting Information, Figure S5). For this reason, measurements are normalized by the images obtained with the microscope, without sample.[18,23,27] In polar-CGM, a reference interferogram, without sample, is acquired and processed exactly as the object interferogram, and the resulting intensity and wavefront images, I_{ref} and w_{ref}, are used to normalize any subsequent intensity and wavefront images of objects, I_{obj} and w_{obj}. More precisely, the wavefronts are subtracted, $W = w_{obj} - w_{ref}$, and the intensity images are divided, $T = I_{obj}/I_{ref}$.[55]

To illustrate the numerical procedure hereinafter, we show measurements on a canonical system, namely a periodic square array ($20 \times 20\ \mu m^2$) of gold nanorods (80 nm long and 40 nm wide) (Figure 1c and Section S3-1). The nanoparticle array exhibits a subwavelength periodicity so that its optical response can be considered continuous, thereby forming a metasurface.[59] Due to the anisotropy of the nanorods, this metasurface exhibits polarization-dependent properties: a longitudinal localized plasmon resonance (LPR) at 630 nm and a transverse LPR at 505 nm (Figure S8). The presence of resonances makes this system rich, in particular, in terms of phase response.

Interferogram Processing

All the polar-CGM image processing methods described below are provided in a public repository.[60] A code example is provided in Section S19. Any image acquired with a 4-polarization camera can be decomposed into 4 subimages corresponding to the 4 axes of the linear micropolarizers of the camera, at 0°, 45°, 90° and 135°, a procedure called demosaicing (see Section S1 for details).

We define the 4 unit vectors $\mathbf{u}_j$, $j \in [1, 4]$, aligned with the 4 orientations of micropolarizers of the sensor, respectively at 0°, 45°, 90°, and 135°, as below (see Figure 1b).

The 4 subinterferograms, processed using the standard QLSI algorithm described in refs 46 and 55 give rise to 8 images: 4 intensity images T_j, and 4 wavefront images W_j, corresponding to the 4 linear polarizations indexed by $j \in [1, 4]$ (Figure 1d−f). The measured phase images are defined as $\Phi_j = \frac{2\pi}{\lambda} W_j$, where λ is the illumination wavelength. The wavefront shift is on the order of 20 nm, that is approximately $\lambda/25$. The noise level is on the order of 0.2 nm ($<\lambda/2000$), achieved with an exposure time of 3 s.

Single-Shot Full-Stokes and Jones Vector Imaging

In this study, like with any Jones matrix imaging method, we restricted ourselves to the study of polarization elements without depolarization, an approximation that is valid when considering 2D nanophotonic samples, because they are static and do not exhibit multiple scattering, like a thick sample. In this case, the Jones formalism is the appropriate approach and the actual Jones vector field $\mathbf{E} = (E_1, E_3)$ in the image plane can be simply retrieved from the measured intensity I_j and wavefront w_j images (see Section S4 eq S5). While this demonstrates the ability of polar-CGM to perform Jones vector imaging in the most general case, this absolute complex electric field is not the quantity of interest in the case of microscopy experiments. As explained above, the intensity and wavefront/phase images need to be normalized by a reference acquisition, without sample. In this way, polar-CGM measures the *relative*

Downloaded from pubs.acs.org/ancac3/article-pdf/20/42/28193/6887672/acsnano.6c06635.pdf by guest on 06 November 2026

https://doi.org/10.1021/acsnano.6c06635
ACS Nano 2026, 20, 28193−28206

Jones vector image, i.e. the image that would be obtained if the microscope were perfect (Section S2, Figure S5).

In the following, although it is not a restriction, we shall consider a *circularly polarized* incident light, first because it simplifies the formalism, then because it is the type of illumination we use hereinafter for Jones *matrix* imaging. A circularly polarized incident illumination reads in the image plane

$$\mathbf{E}_0 = \frac{1}{\sqrt{2}} E_0(\mathbf{u}_1 - hi\mathbf{u}_3) \tag{3}$$

where $E_0 = |\mathbf{E}_0|$, and $h = +1$ or -1, respectively for right-handed circular polarization (RCP) and left-handed circular polarization (LCP).

In the presence of an object, the electric field $\mathbf{E}$ and the electric field $\mathbf{e}$ normalized by the incident field read

$$\mathbf{E}(\mathbf{r}) = E_1(\mathbf{r})\mathbf{u}_1 + E_3(\mathbf{r})\mathbf{u}_3 \tag{4}$$

$$\mathbf{e}(\mathbf{r}) = (e_1(\mathbf{r})\mathbf{u}_1 + e_3(\mathbf{r})\mathbf{u}_3)/\sqrt{2} \tag{5}$$

where

$$\mathbf{E}(\mathbf{r}) = E_0\mathbf{e}(\mathbf{r}) \tag{6}$$

$$E_j(\mathbf{r}) = E_0 \mathrm{e}_j(\mathbf{r})/\sqrt{2} \tag{7}$$

$$\mathrm{e}_j(\mathbf{r}) = |\mathrm{e}_j(\mathbf{r})|\exp[i(\phi_j(\mathbf{r}) - h(j-1)\pi/4)] \tag{8}$$

where $\mathbf{r} = (x, y)$ and ϕ_j, $j \in [1, 4]$, are the phase maps. With these notations, the absence of any object corresponds to $|\mathrm{e}_j| = 1$ and $\phi_j = 0$, $\forall j \in [1, 4]$.

The normalized electric field $\mathbf{e}(\mathbf{r})$ can be expressed as a function of the measured wavefront W_j and normalized intensity T_j images as

$$\mathbf{e}(\mathbf{r}) = \sqrt{\frac{T_1(\mathbf{r})}{2}} \exp\left[i\left(\frac{2\pi W_1(\mathbf{r})}{\lambda} - \delta\phi_1\right)\right]\mathbf{u}_1 + \sqrt{\frac{T_3(\mathbf{r})}{2}} \exp\left[i\left(\frac{2\pi W_3(\mathbf{r})}{\lambda} - \delta\phi_3 - h\pi/2\right)\right]\mathbf{u}_3 \tag{9}$$

The measured images $\Phi_j = 2\pi W_j/\lambda$ do not exactly correspond to the phase maps ϕ_j as defined in eq 8. There are undetermined offsets $\delta\phi_j$ because QLSI provides phase (or wavefront) images up to an arbitrary constant. These undetermined offsets arise from the fact that QLSI primarily measures wavefront *gradients*, which are subsequently integrated to reconstruct the wavefront image, leading to an integration constant. These offsets can be determined by taking advantage of the measurements of the intensity and wavefront images at ± 45° (T_2, T_4, W_2, W_4), which were not involved so far (Section S4). We call this method the quadrature offset correction (QOC). This procedure retrieves the phase difference $\delta\phi_1 - \delta\phi_3$, but not the absolute phase, which is not relevant anyway when imaging a light field: A global phase offset just amounts to changing the origin of time. The other method consists of setting the offset of the wavefront images so that the wavefront equals zero in areas where there is no object. We call this second method the set-offset-on-clear-area (SOCA) method. We can apply the SOCA method in the case of the array of gold nanorod samples (Figure 1f), since empty areas are visible within the field of view.

From these measurements, one can extract the maps of the Stokes parameters normalized with respect to the incident field E_0, S_0, S_1, S_2, S_3 defined by

$$\begin{cases} S_0 &= (|\mathrm{e}_1|^2 + |\mathrm{e}_3|^2)/2 \\ S_1 &= (|\mathrm{e}_1|^2 - |\mathrm{e}_3|^2)/2 \\ S_2 &= \mathrm{Re}(\mathrm{e}_1\mathrm{e}_3^*) = (|\mathrm{e}_2|^2 - |\mathrm{e}_4|^2)/2 \\ S_3 &= \mathrm{Im}(\mathrm{e}_1\mathrm{e}_3^*) \end{cases} \tag{10}$$

The factor of 1/2 compared to the standard definitions comes from the $1/\sqrt{2}$ convention in the definition of e_j (see eq 5) and ensures that $S_j \in [-1, 1]$. Note the two possible expressions of S_2, one arising from the measured T_1, T_3, W_1, and W_3 images, and the other one arising only from the T_2 and T_4 measurements (when the SOCA method is applied). These two approaches to extracting the coefficient S_2 from the set of 8 initial images highlight some redundancy present in the acquired data. Indeed, a camera with only 3 polarized pixels at 0, 45, and 90° would be enough in theory (but complex to design). This redundancy can be exploited as a means to retrieve the Jones vector field, as explained above, or, when using the SOCA method, it can be used to improve the signal-to-noise ratio by averaging the images. But more interestingly, it can also be used to determine the grating-camera distance. Indeed, the relation $S_2 = \mathrm{Re}(e_1 e_3^*)$ requires the determination of the phase relation between the components e_1 and e_3, and this phase is incorrect if the wavefront maps are incorrect, i.e., if the camera-grating distance is not properly determined. Therefore, in polar-CGM, the camera-grating distance can be easily determined by making the two values of S_2 consistent with each other. This technique, which we call the S_2 test, is detailed in Section S7.

For fully polarized light, which is the assumption in this study, we also have the relation $S_0^2 = S_1^2 + S_2^2 + S_3^2$. This expression and what we discussed above give another set of expressions of S_j that involve only intensity measurements (except for the handedness h)

$$\begin{cases} S_0 &= (T_1 + T_3)/2 \\ S_1 &= (T_1 - T_3)/2 \\ S_2 &= (T_2 - T_4)/2 \\ S_3 &= h\sqrt{S_0^2 - S_1^2 - S_2^2} \end{cases} \tag{11}$$

The polarization ellipse is a common visual way to describe the polarization state of a light wave, at a specific location. Its geometrical properties, defined in Section S6, can be retrieved using the following expressions

$$\begin{cases} A &= \sqrt{\frac{1}{2}(S_0 + |L|)} \\ B &= \sqrt{\frac{1}{2}(S_0 - |L|)} \\ \theta_e &= \frac{1}{2}\arg(L) \\ \epsilon &= \tan\eta_e = h\frac{B}{A} \end{cases} \tag{12}$$

https://doi.org/10.1021/acsnano.6c06635
ACS Nano 2026, 20, 28193−28206

Downloaded from pubs.acs.org/ancac3/article-pdf/20/42/28193/6887672/acsnano.6c06635.pdf by guest on 06 November 2026

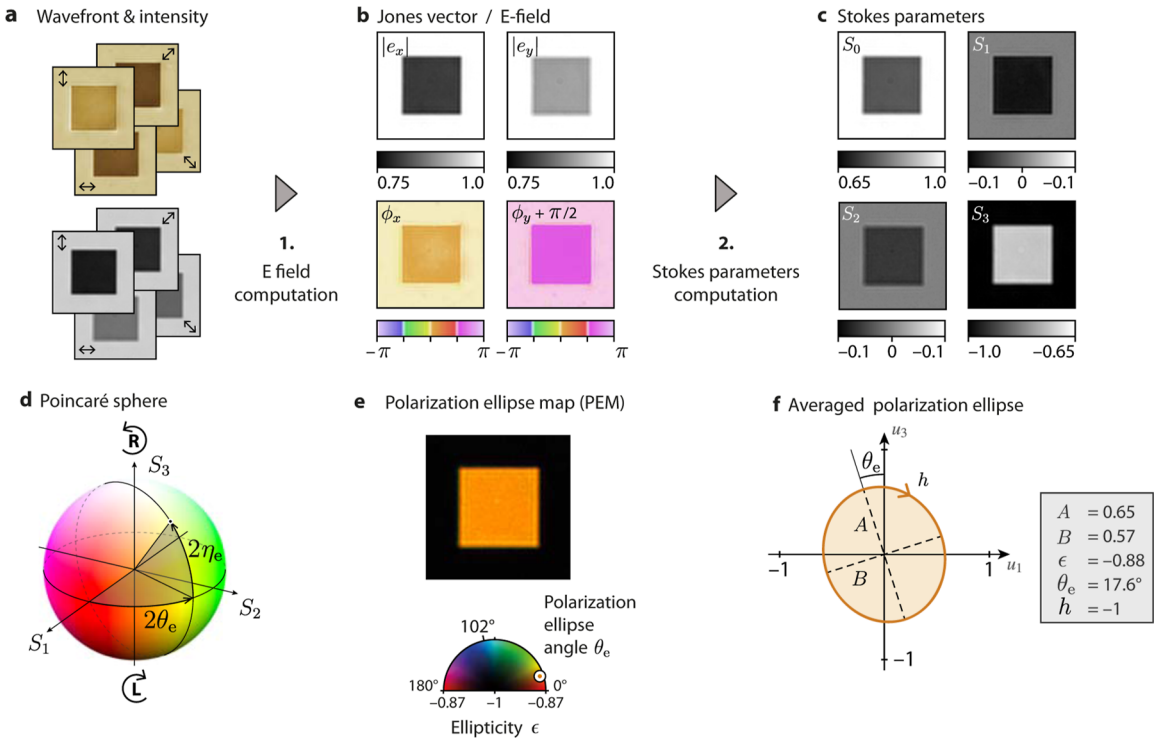


Figure 2. Retrieval of the light field at the image plane created by a square metasurface made of gold nanorods, illuminated under LCP, at λ = 510 nm. (a) 4 wavefront images and 4 normalized intensity images extracted from one interferogram (see Figure 1d–f). (b) Jones vector images represented by the amplitude and phase of the two components of the electric field. (c) Images of the Stokes parameters. (d) Poincaré sphere showing the Stokes parameters and defining the polarization angle θ_e and the ellipticity angle η_e. (e) Polarization ellipse map. (f) Drawing of the averaged polarization ellipse, along with the averaged property values of the polarization ellipse over the metasurface.

where $L = S_1 + iS_2$ and $h = \text{sign}(S_3)$. θ_e is the polarization ellipse angle, ϵ the ellipticity, η_e is the ellipticity angle, and A and B are the semimajor and semiminor axes. $\eta_e = 0$ ($\epsilon = 0$) for a linear polarization, $\eta_e = \pi/4$ (i.e., $\epsilon = 1$) for an RCP and $\eta_e = -\pi/4$ (i.e., $\epsilon = -1$) for an LCP.

According to eq 11, the Stokes parameters, and thus the ellipse properties (eq 12), could be retrieved only from intensity measurements T_j. This means that determining the polarization state of a fully polarized beam requires neither QLSI nor any QPI measurement. It can be retrieved using a simple 4-polarization camera, without actual phase measurement. One can even derive expressions of the complex electric field from S_j measurements

$$e_1 = \sqrt{S_0 + S_1} \tag{13}$$

$$e_3 = \frac{S_2 - iS_3}{\sqrt{S_0 + S_1}} \tag{14}$$

However, these components of the electric field, obtained using intensity-only measurements, are missing precious pieces of information: (i) the handedness h of the field, i.e. the sign of S_3, as stated above, and more importantly, (ii) the phase relation from one pixel to another in the image, i.e., the phase map. All the e_1 components of the image are real numbers, according to eq 13. As a consequence, only the phase difference between the two orthogonal components is determined, $|\phi_1(\mathbf{r}) - \phi_3(\mathbf{r})|$, but not their absolute phase values $\phi_1(\mathbf{r})$ and $\phi_3(\mathbf{r})$. The added value of QLSI is to provide this missing information. First, QLSI provides the proper phase relation between all the pixels in the image. Second, if an object-free area can be found in the field of view, the SOCA method provides the overall phase shift of the image compared to the incoming field. This phase information is mandatory for computing and mapping the optical properties of nanomaterials, as explained further. Finally, the use of a QLSI grating also resolves the indeterminacy of the handedness h. If the actual handedness of the incident light is not properly chosen in the algorithm, the computations of the Stokes parameters S_j using eqs 10 and 11 are inconsistent, as demonstrated in Section S7.

Figure 2 illustrates the retrieval of the polarization images from the set of 8 wavefront and intensity images shown in Figure 1f. These wavefront and intensity images were processed using eq 9 to obtain the 4 fields fully defining the complex vectorial electric field, that is, the amplitude and phase images, shown in Figure 2b. Stokes parameters were computed using eq 11 (Figure 2c). The value of S_3 outside the array is −1, indicating LCP illumination. h was determined using the S_2 test (see Section S7). Systematically showing 4 images would be cumbersome. In many occasions later on, we will rather show what we call the polarization ellipse map (Figure 2e). In such a map, the color (hue) codes the direction of the long axis of the ellipse (θ_e) and the color brightness (value) codes the ellipticity (ϵ) over a range indicated in the associated color map, below the image. Figure 2f shows the properties of the polarization ellipse, averaged over the metasurface. Somewhat counterintuitively, the orientation of the ellipse (17.6°) is not aligned with the symmetry axes of the nanorods, the nanorod long axis being vertical in the images. This symmetry breaking arises from the use of circularly polarized light and is a sign of birefringence. The exact same effect

Downloaded from pubs.acs.org/ancac3/article-pdf/20/42/28193/6887767/2/acsnano.6c06635.pdf by guest on 06 November 2026

https://doi.org/10.1021/acsnano.6c06635
ACS Nano 2026, 20, 28193−28206

appears when a circularly polarized light passes through a quarter wave plate: the polarization becomes linear with an axis that is not aligned with the main axes of the wave plate (see Section S15 for details). The precision of all these measurements is confirmed by the uniformity of the images and their low noise level.

Jones Matrix Imaging

The interest in characterizing a light beam is 2-fold: either to gain knowledge about the light source itself (as in astronomy or laser beam characterization), or to retrieve information related to an object with which the beam has interacted (as in optics testing or in microscopy). The latter is the topic of this section.

In microscopy, performing polarization measurements is appropriate when the sample of interest is anisotropic, such as elongated or chiral nanoparticles, dichroic or birefringent materials. In these cases, the physical quantities that describe the optical properties of matter are tensorial in nature. In the following, we explain how polar-CGM can retrieve these tensorial optical properties, in particular, in the case of dense arrays of nanoparticles, i.e. metasurfaces.

The optical properties of a planar object lying in the sample plane of a microscope can be described using the Jones formalism and the simple relation (see Figure S15)

$$\mathbf{e}(x, y) = \mathbb{J}(x, y)\mathbf{e}_0 \tag{15}$$

where $\mathbf{e}_0$ is the Jones vector of the illumination beam at the image plane (assumed to be uniform), which is transformed into the Jones vector $\mathbf{e}(x, y)$ by the Jones matrix $\mathbb{J}(x, y)$, which fully characterizes the object.

In practice, the only unknown in this relation is $\mathbb{J}(x, y)$, because the incident polarization state $\mathbf{e}_0$ is controlled and the transmitted field $\mathbf{e}(x, y)$ is the measured quantity (as detailed in the previous section). However, measuring a Jones vector $\mathbf{e}(x, y)$ is equivalent to measuring 2 complex numbers, while a Jones matrix is composed of 4 complex numbers. There is more information in $\mathbb{J}$ than in one measurement of $\mathbf{e}$. Consequently, in principle, the complete characterization of the optical properties of a material cannot be achieved from a single measurement of the transmitted field for a given incident illumination, regardless of the technique used. For this reason, several measurements of $\mathbf{e}$ corresponding to several illumination modalities $\mathbf{e}_0$ should be performed to retrieve $\mathbb{J}$. Let us call the $\{\mathbf{e}_0^k\}_{k\in[1,N]}$ the N illumination fields used to acquire the N field measurements $\{\mathbf{e}^k\}_{k\in[1,N]}$. Let us define the matrix $\mathcal{E}_0 = [\mathbf{e}_0^1 \dots \mathbf{e}_0^N] \in \mathbb{C}^{2\times N}$ and $\mathcal{E} = [\mathbf{e}^1 \dots \mathbf{e}^N] \in \mathbb{C}^{2\times N}$ composed of the horizontal concatenation of Jones vectors. Then, the Jones matrix can be recovered in a simple and elegant way as (see the derivation in Section S8)

$$\mathbb{J} = \mathcal{E}\mathcal{E}_0^\dagger(\mathcal{E}_0\mathcal{E}_0^\dagger)^{-1} \tag{16}$$

where $\mathcal{E}^\dagger$ denotes the conjugate-transpose of $\mathcal{E}$. When one measurement is made ($N = 1$), the rank of $\mathcal{E}_0$ is 1, and the matrix $\mathcal{E}_0\mathcal{E}_0^\dagger$ is not invertible. Equation 16 cannot be used, which is consistent with the statement above that one measurement is not sufficient to determine $\mathbb{J}$. One needs at least two measurements with two independent illuminations to determine $\mathbb{J}$ from eq 16. We recommend performing two measurements for LCP and RCP illuminations, $\mathbf{e}_0^{\mathrm{L}} = \frac{1}{\sqrt{2}}\begin{pmatrix}1\\ i\end{pmatrix}$ and $\mathbf{e}_0^{\mathrm{R}} = \frac{1}{\sqrt{2}}\begin{pmatrix}1\\ -i\end{pmatrix}$. In that case, $\mathcal{E}_0 = [\mathbf{e}_0^{\mathrm{L}}\mathbf{e}_0^{\mathrm{R}}] = \frac{1}{\sqrt{2}}\begin{pmatrix}1 & 1\\ i & -i\end{pmatrix}$, and $\mathcal{E} = [\mathbf{e}^{\mathrm{L}}\mathbf{e}^{\mathrm{R}}] = \begin{pmatrix}\mathrm{e}_1^{\mathrm{L}} & \mathrm{e}_1^{\mathrm{R}}\\ \mathrm{e}_3^{\mathrm{L}} & \mathrm{e}_3^{\mathrm{R}}\end{pmatrix}$. In this way, $\mathbb{J}$ could be properly recovered. However, the fields $\mathbf{e}^{\mathrm{L}}$ and $\mathbf{e}^{\mathrm{R}}$ arise only from the 0° and 90° pixels of the camera. The information originating from the 45° and 135° pixels would be discarded. Interestingly, eq 16 enables the integration of this information, by considering this missing information as separate measurements and including them in eq 16 to obtain 2×4 matrices

$$\mathcal{E}_0 = \frac{1}{\sqrt{2}}\begin{pmatrix}1 & 1 & 1 & 1\\ i & -i & i & -i\end{pmatrix} \tag{17}$$

$$\mathcal{E} = \begin{pmatrix}\mathrm{e}_1^{\mathrm{L}} & \mathrm{e}_1^{\mathrm{R}} & \mathrm{e}_2^{\mathrm{L}} & \mathrm{e}_2^{\mathrm{R}}\\ \mathrm{e}_3^{\mathrm{L}} & \mathrm{e}_3^{\mathrm{R}} & \mathrm{e}_4^{\mathrm{L}} & \mathrm{e}_4^{\mathrm{R}}\end{pmatrix} \tag{18}$$

Using these matrices in eq 16 enables the processing of all the information acquired by the camera, leading to more precise measurements of the Jones matrix maps.

Metasurfaces are 2-dimensional and are necessarily homogeneous polarization objects for this reason, meaning that the eigenvectors of their Jones matrix are orthogonal.[31] In the orthogonal vector basis, the Jones matrix can be written as

$$\mathbb{J}_0 = \begin{pmatrix}t_{\mathrm{o}} & 0\\ 0 & t_{\mathrm{e}}\end{pmatrix} = \begin{pmatrix}\rho_{\mathrm{o}}\mathrm{e}^{\mathrm{i}\Delta_{\mathrm{o}}} & 0\\ 0 & \rho_{\mathrm{e}}\mathrm{e}^{\mathrm{i}\Delta_{\mathrm{e}}}\end{pmatrix} \tag{19}$$

where t_0 and t_{e} are the complex transmittances of the eigenstates. Importantly, the polarization eigenstates of a general metasurface are not necessarily linear. In particular, chiral metasurfaces can exhibit elliptical eigenstates associated with circular dichroism and optical activity. Although polar-CGM is fully capable of retrieving such states, we deliberately leave them outside the scope of the present study. First, a proper treatment of chiral samples would require substantial additional analysis and discussion. Second, chirality constitutes a broad and active research field in its own right, and we believe that a subsequent dedicated article explicitly focused on chiral samples would provide a clearer and more impactful contribution to this community. To keep the present study focused on the core principles and experimental validation of the method, we therefore restrict our analysis to achiral metasurfaces. In this case, the Jones matrix remains symmetric and its eigenstates are not only orthogonal but also linearly polarized. The extension to chiral metasurfaces will be addressed in future work.

In eq 19, $\rho_{\mathrm{o}} \neq \rho_{\mathrm{e}}$ denotes linear dichroism (LD), usually quantified by the diattenuation D

$$D = \frac{\rho_{\mathrm{o}} - \rho_{\mathrm{e}}}{\rho_{\mathrm{o}} + \rho_{\mathrm{e}}} \tag{20}$$

The case $\Delta_{\mathrm{o}} \neq \Delta_{\mathrm{e}}$ denotes linear birefringence (LB), which means that the two eigenstates experience different refractive indices. LB is quantified by the birefringence angle that reads

$$\beta = \Delta_{\mathrm{o}} - \Delta_{\mathrm{e}} \tag{21}$$

with $t_0 = |t_0|\mathrm{e}^{\mathrm{i}\beta/2}$ (fast axis) and $t_{\mathrm{e}} = |t_{\mathrm{e}}|e^{-\mathrm{i}\beta/2}$ (slow axis).

The eigen transmittances contain all the intrinsic optical properties of the metasurface. However, they are related to the transmitted electric field, that is, the sum of the incident field

Downloaded from pubs.acs.org/ancac3/article-pdf/20/42/28193/6887767/2/acsnano.6c06635.pdf by guest on 06 November 2026

https://doi.org/10.1021/acsnano.6c06635
ACS Nano 2026, 20, 28193−28206

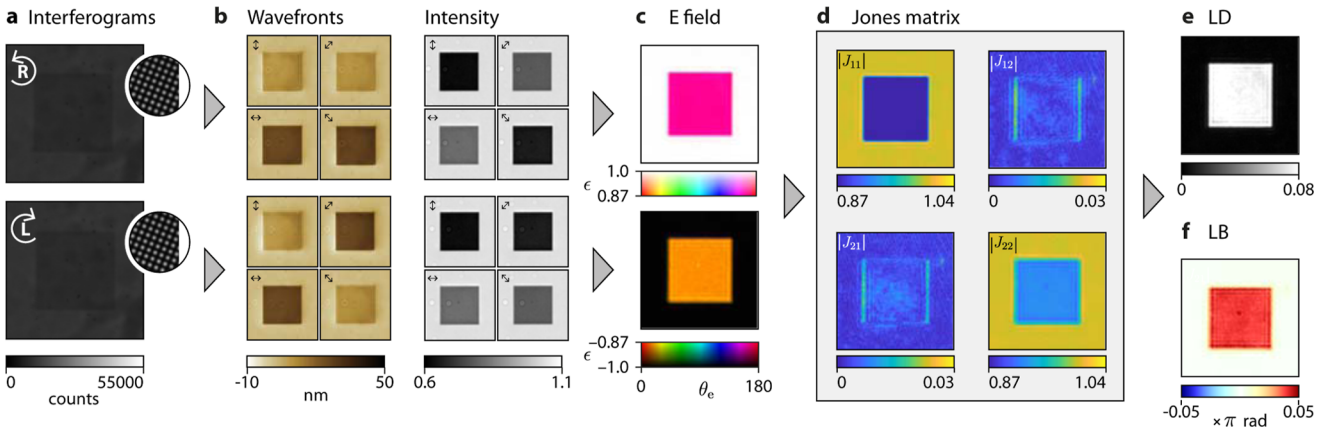


Figure 3. Jones matrix imaging of a uniform array of gold nanorods, illuminated at λ = 510 nm. (a) Two raw interferograms acquired under LCP and RCP illuminations. (b) 4 wavefront images $W_j(\mathbf{r})$ and 4 intensity images $T_j(\mathbf{r})$ extracted from each interferogram by demosaicing and QLSI processing. (c) Complex electric field amplitudes $\mathbf{e}^L(\mathbf{r})$ and $\mathbf{e}^R(\mathbf{r})$ of the light wave computed from the wavefront and intensity images (b). (d) Images of the 4 coefficients of the Jones matrix $\mathbb{J}(\mathbf{r})$ computed from (c). Only the moduli are displayed, not the arguments, for simplicity. (e) Linear dichroism map and (f) linear birefringence map computed from the Jones Matrix. An animated version of this figure, for various sample rotation angle values, is provided in Section S16.

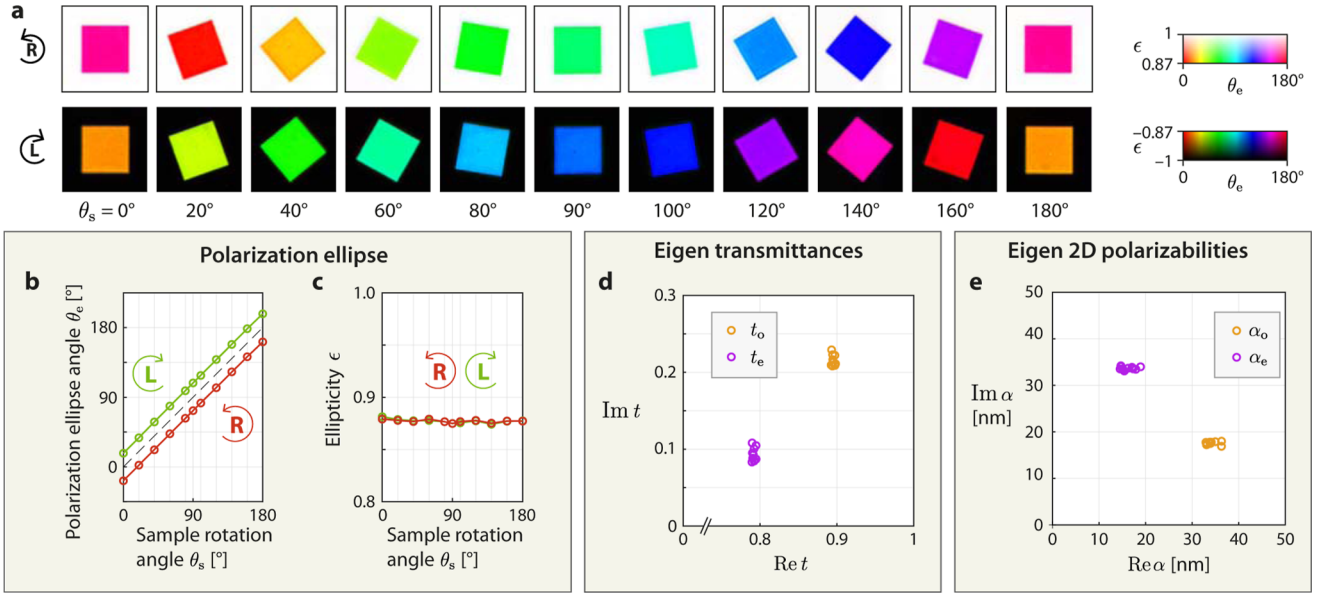


Figure 4. Characterization of uniform metasurfaces as a function of their rotation angle. (a) Polarization ellipse maps of the metasurfaces for various sample orientations, both for LCP and RCP incident illuminations. (b) Orientation of the polarization ellipse averaged over the metasurface area, both for LCP and RCP incident polarizations, as a function of the sample orientation. (c) Corresponding ellipticity. (d) Eigen transmittances t_0 and t_e of the metasurfaces measured for all the metasurface rotation angles. (e) Corresponding eigen 2D polarizabilities α_o and α_e, calculated from eq 22.

and the scattered field. Characterizing the scattered field only, in amplitude and phase, is also meaningful, as it is a closer description of the response of the imaged object itself. For this purpose, one can rather consider the 2D polarizability, defined in Section S13

$$\alpha_{o,e} = \frac{i\lambda}{\pi}(1 - t_{o,e}) \tag{22}$$

which quantifies the induced surface polarization relative to the incident field. If the main axes of the anisotropic object (i.e., the eigenstates) are rotated compared with the axes (u_1, u_3) used to express the Jones matrices, then the Jones matrix of the homogeneous object reads

$$\mathbb{J} = \mathbb{R}(-\psi)\mathbb{J}_0\mathbb{R}(\psi) \tag{23}$$

where $\mathbb{R}$ is the rotation matrix and ψ is the rotation angle of the ordinary axis of the object from (u_1). The Jones matrix of a homogeneous object with linear birefringence and diattenuation has 5 independent parameters (instead of 8 in the general case), making the use of a single measurement of the electric field $\mathbf{e}$ still not sufficient (only 4 parameters).

Complex transmittances t_0 and t_e can be directly estimated by computing the eigenvalues of the Jones matrix $\mathbb{J}$ in eq 23. In an ideal case where the model (23) is exact (no noise and perfect linear homogeneous sample), the angle ψ is directly deduced from the polar coordinates of the leading eigenvector of $\mathbb{J}$. However, noise can make eq 23 inaccurate even with a perfect linear homogeneous sample. Therefore, in practice, to improve precision, we can first project the Jones matrix

https://doi.org/10.1021/acsnano.6c06635
ACS Nano 2026, 20, 28193−28206

Downloaded from pubs.acs.org/ancac3/article-pdf/20/42/28193/6887767/2/acsnano.6c06635.pdf by guest on 06 November 2026

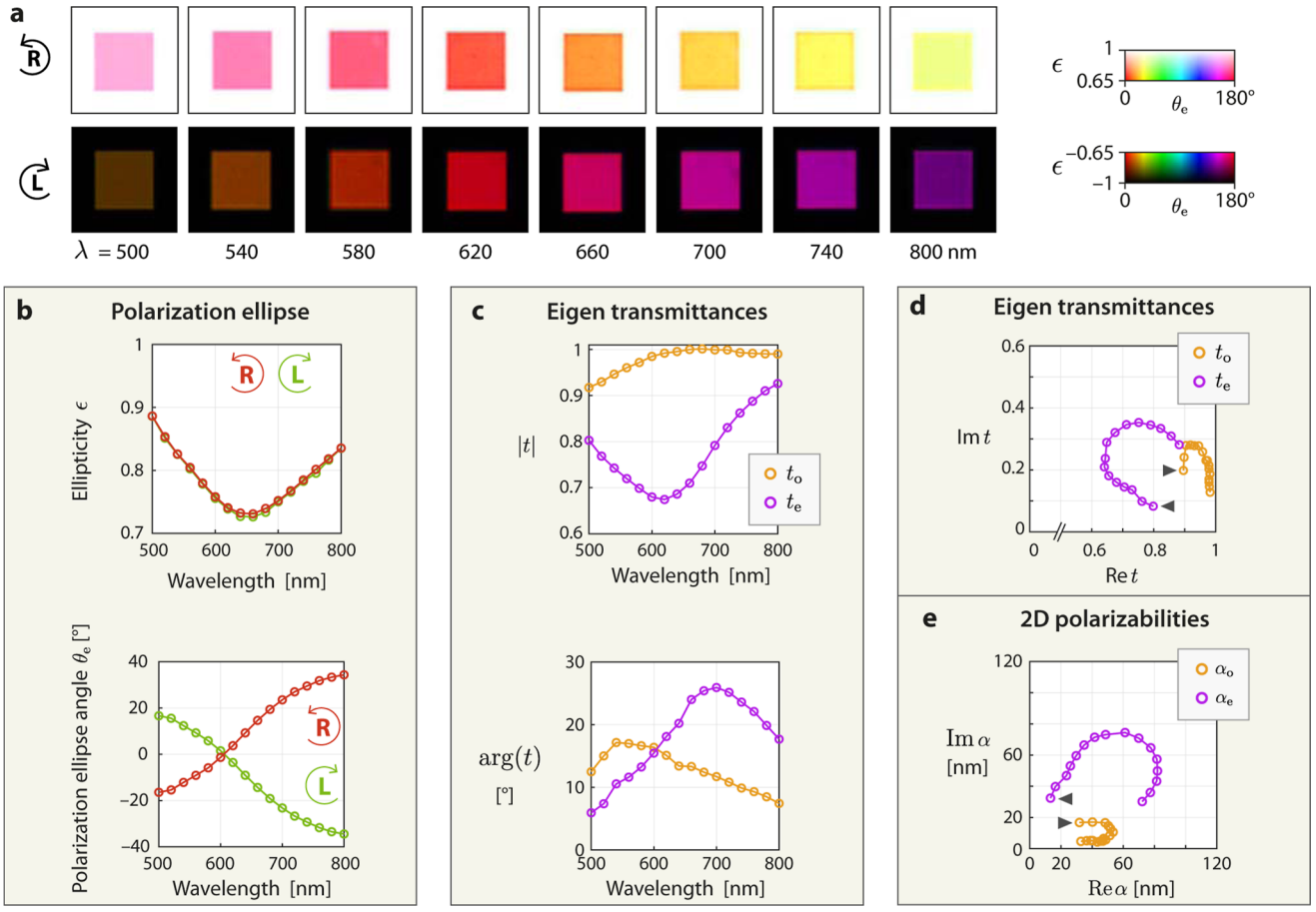


Figure 5. Spectral characterization of a metasurface, from 500 to 800 nm. (a) Polarization ellipse images at various wavelengths, for incident LCP and RCP. (b) Ellipticity and polarization ellipse angle averaged over the area of the metasurface, for incident LCP and RCP. (c) Modulus and argument of the eigen transmittances. (d) Eigen transmittances in the complex plane. (e) Eigen 2D polarizabilities in the complex plane.

obtained through eq 16 onto the set of linear homogeneous Jones matrices before computing its spectral decomposition. The full procedure is detailed in Section S9 for completeness. This algorithm is not a requirement. If there is any doubt as to whether the sample may exhibit optical activity, this algorithm should not be used, and the complex transmittances t_o and t_e can be directly estimated by computing the eigenvalues of the Jones matrix.

Finally, it should be noted that the Mueller matrix could also be retrieved from the Jones matrix (Section S11). Mueller imaging remains of limited interest for 2D nanophotonic samples because it cancels the information on the global phase in each pixel, which is still relevant information, as explained above. The consequence is that it cannot predict light propagation above the metasurface. Furthermore, the main purpose and advantage of the Mueller matrix compared to the Jones matrix is to provide information on the depolarization of a light beam. However, in principle, 2D samples cannot depolarize light, because they do not exhibit multiple scattering like thick samples. Possible depolarization effects arising from metasurfaces are discussed in Section S12.

We present now experimental results that illustrate the numerical protocol of Jones Matrix retrieval, detailed above. Two interferograms were acquired under LCP and RCP illuminations (Figure 3a), which were treated with a demosaicing and QLSI algorithm to produce 16 wavefront and intensity images (Figure 3b). These images were processed using eq 9 to compute the complex vectorial electric field for both illuminations (Figure 3c). The averaged ellipticity remains unchanged. However, the ellipse angles (17.6° and 162° ≡ −18°) are symmetric compared to the symmetry axes of the sample (0° and 90°), within the uncertainty of the measurement.

From these complex electric field images, the Jones Matrix is computed using eq 16. The map of the Jones matrix is represented by the modulus maps of its 4 components (Figure 3d). Only the modulus, not the phases, are displayed, for simplicity. The nondiagonal terms J_{12} and J_{21} exhibit weak values, because the main axes of the sample are aligned with u_1 and u_3, the basis vectors in which the matrices are expressed. In addition, we provide a movie in which Figure 3 is animated, as a function of the sample rotation angle (Section S16). This movie highlights how the nondiagonal terms become stronger when the sample rotation angle deviates from 0 or 90°.

The effect of the orientation of the sample around the z axis is depicted in Figure 4. Figure 4a displays the polarization ellipse map of the nanorod array at various sample rotation angles θ_s. A constant angle shift of 55° is systematically observed between the right and left polarizations. The presence of a shift is the signature of birefringence. Purely dichroic samples do not exhibit such a shift (see Section S15 for an explanation). These ellipse angles θ_e naturally follow the sample rotation angles θ_s (Figure 4b). The ellipticity of the polarization ellipse remains constant while rotating the sample

https://doi.org/10.1021/acsnano.6c06635
ACS Nano 2026, 20, 28193−28206

Downloaded from pubs.acs.org/ancac3/article-pdf/20/42/28193/6887767/2/acsnano.6c06635.pdf by guest on 06 November 2026

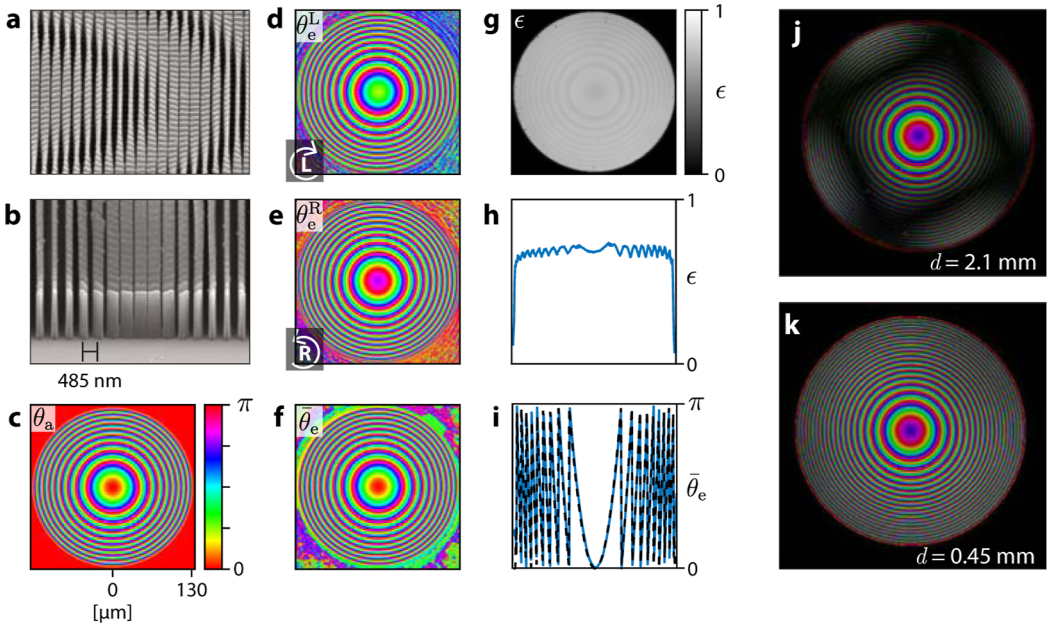


Figure 6. Characterization of a radially symmetric metasurface made of dielectric nanofins, with parameter $c = 3.55 \times 10^{-3}$ μm^{-2}. (a,b) SEM images of the nanofins. (c) Map of the actual orientation θ_a of the nanofins. (d) Measured polarization ellipse orientation θ_e^L for an LCP illumination. (e) Measured polarization ellipse orientation θ_e^R for an RCP illumination. (f) Average of the polarization ellipse orientation maps (d,e), matching the actual nanofin orientation (c). (g) Ellipticity map ϵ. (h) Cross-cut of (g). (i) Cross-cut of (c,f), respectively, with dashed black line and solid blue line. (j) Polarization ellipse map of the metalens with parameter $c = 7.09 \times 10^{-3}$ μm^{-2}, featuring higher spatial frequencies. (k) Same imaged metasurface when the grating is moved from 2.1 to 0.45 mm.

(Figure 4c). These observations demonstrate that the inner properties of the sample are not affected by the rotation of the sample, and validate the accuracy of the approach.

The average complex eigen transmittances t_0 and t_e, extracted from the Jones matrices, are displayed in Figure 4d. Note that all the values for all the sample rotations are displayed, as a means to gauge the precision of the measurements and identify any artifact. All measurements are remarkably overlapped, highlighting the excellent precision of the measurements using polar-CGM for standard metasurfaces.

More meaningful quantities than the eigen transmittances are the 2D polarizabilities α_o and α_e (see eq 22). Their values, for all sample orientations, are represented in Figure 4e. α_o corresponds to the longitudinal response of the nanorods, while α_e corresponds to the transverse response. Interestingly, at the wavelength used experimentally, $\lambda = 510$ nm, only the transverse response is excited at its LPR, corresponding to α_e, which exhibits a large phase shift of approximately $\pi/3$. The behavior of a common oscillator is almost retrieved: We do not observe a phase shift of $\pi/2$ at resonance due to interband transitions that involve more mobile electrons (other resonances) that damp the response. The longitudinal polarizability features a larger modulus (consistently with the spectrum in Figure S8), and a reduced phase shift since the resonance is further away (630 nm). Here is how the measured 2D polarizabilities can provide insight into the physical mechanisms underlying the response of the metasurface.

Unlike other QPI approaches, CGM does not require a coherent laser source, making it easier to tune the illumination wavelength using, for example, a monochromator, a set of LEDs, or a white-light laser. Figure 5 illustrates the capability of polar-CGM to perform spectroscopic measurements. Figure 5a shows various polarization ellipse images of the nanorod metasurface acquired over the visible spectral range. The values of θ_e for RCP and LCP illuminations differ (5b), indicating that the metasurface exhibits a combination of birefringence and dichroism, except for a specific wavelength of approximately 610 nm, where the polarization ellipse is aligned with a symmetry axis of the metasurface ($\theta_e = 0$), indicating pure dichroism. This particular behavior is also observed in the argument of the two complex transmittances shown in Figure 5c, which coincide at this wavelength. The plots of the transmittances and polarizabilities (Figure 5d,e) exhibit a characteristic circular arc, which is a hallmark of a resonance. The polarizability provides a more intuitive representation of the resonance, as its trajectory forms a circular arc close to the origin, rather than around (1,0) as in the complex transmittance plot. These data are compared with numerical simulations (Section S14). The simulations correctly reproduce the trajectories of the eigen transmittances $t_{o,e}(\lambda)$ in the complex plane. A slight discrepancy in amplitude is observed presumably due to uncertainties in the Ti layer thickness.

We now present results obtained for more complex and practically relevant metasurfaces, consisting of nonuniform, circular, dense arrays of asymmetric meta-atoms (Figure 6a). This time, the meta-atoms are polymer (dielectric) nanofins (Figure 6b) (see Section S3−2 for fabrication details).[61] They are all identical, but exhibit various rotation angles about (z), $\theta_a(x, y)$. Throughout the metasurfaces, the orientations of the nanofins depend quadratically, and only, on the radial coordinate r

$$\theta_a(r) = \frac{1}{2} c r^2 \tag{24}$$

as depicted in Figure 6c. $c = 3.55 \times 10^{-3}$ μm^{-2} for the results presented in Figure 6a−j. In the center of the metasurface, the orientation of the nanofins is horizontal (along (x), $\theta_a(0) = 0$).

Downloaded from pubs.acs.org/ancac3/article-pdf/20/42/28193/6887767/2/acsnano.6c06635.pdf by guest on 06 November 2026

https://doi.org/10.1021/acsnano.6c06635
ACS Nano 2026, 20, 28193−28206

Polar-CGM measurements are shown in Figure 6d,e, which represent the polarization ellipse orientation maps for the LCP and RCP illuminations, respectively. These orientation maps do not match the actual orientation of the nanofins θ_a displayed in Figure 6c, for the reason explained earlier. However, they differ from θ_a by ±45°. In particular, at the center of the metasurface, the measured orientations of the polarization ellipse are almost orthogonal, equal to $\theta_e^L = 41.1°$ and $\theta_e^R = -39.1°$, within the uncertainty of the measurement. This is a sign of an almost purely birefringent metasurface, in agreement with the dielectric nature of the nanofins, with weak absorption (see Section S15). The average $\overline{\theta}_e$ of these two orientation maps, corresponding to RCP and LCP illumination, is shown in Figure 6f. This map corresponds to the actual nanofin orientation map (Figure 6c). The cross sections of these two maps are plotted in Figure 6i, showing perfect agreement. This is how the nanofin orientations can be simply retrieved experimentally.

Figure 6g shows the ellipticity map for RCP illumination (the one for LCP is identical), along with its cross-section (Figure 6h). The ellipticity should be perfectly uniform, as a rotation of a nanofin only leads to a rotation of the polarization ellipse, not a variation of its shape. Any nonuniformity reveals deviation from a perfect metasurface, which can come from fabrication imperfections. Here, the weak modulation of the ellipticity observed in Figure 6h is attributed more to the close-proximity effect between neighboring nanofins. Indeed, the environment of the nanofins depends on their orientation θ_a as can be seen in the SEM images (Figure 6b,c). Polar-CGM can be used to detect such experimental deviations from an ideal metasurface.

Imaging a metasurface by polar-CGM fundamentally amounts to imaging a grating with a grating. This scheme can lead to an issue that is highlighted in Figure 6j,k, and we explain here its origin and how to solve it. The use of such circular metasurfaces with a regular variation of the spatial frequencies along the radial coordinates is convenient to test the spatial resolution limits of polar-CGM. In Figure 6j, a metasurface with a higher fringe frequency ($7.09 \times 10^{-3}\ \mu m^{-2}$) was used, leading to artifactual dark fringes. In QLSI, the bright spot array on the interferograms (Figure 1d) can be understood as the interference between 4 image replicas that propagated along the ±1 diffraction orders of the cross-grating. Problems occur in QLSI when the shear distance between each pair of images is equal to half the period of the imaged periodic object. In that case, the fringes are blurred. This condition gives rise to the following relation that tells which periods in the image are blurred

$$p_j = \frac{4d\lambda}{jM\Gamma},\ j \in \mathbb{N}^* \tag{25}$$

This equation explains the presence and positions of the dark fringes in Figure 6j. According to eq 25, this problem can always be solved by reducing the distance d that separates the grating from the camera. The following criterion can even be derived to ensure the absence of such artifacts: the grating-to-camera distance must be smaller than ten times the QLSI grating pitch (see Section S17 for the derivation). Accordingly, in Figure 6k, the fringes were removed by reducing the grating distance from d = 2.1 to 0.45 mm. More detail on this effect is provided in Section S17.

CONCLUSIONS

In conclusion, we have reported polar-CGM, a simple and versatile microscopy approach enabling the single-shot retrieval of the full complex vectorial electromagnetic field, and the two-shot retrieval of the polarization properties of a sample. We illustrated the interest of the technique with the characterization of vectorial metasurfaces, which represent controlled and arbitrarily complex samples. This work lies in the field of polarimetric microscopy, which now encompasses a wide range of approaches, most of them developed over the past decade, motivated by applications in biology and nanophotonics. To compare polar-CGM with these techniques we propose six criteria: (i) simplicity, (ii) single-shot capability, (iii) chromaticity, (iv) noise, (v) cost, and (vi) image definition, which we discuss below.

In terms of simplicity (i), polar-CGM offers a compact design that requires only minimal alignment, making it a camera-like add-on to a microscope. This benefit contrasts with DHM-based approaches, where the whole microscope should be modified, or with approaches based on the mechanical motion of polarizing optical elements.[19−21,24,25,29] Our current system remains bulky because of the use of a relay-lens, but could be made much more compact by attaching the QLSI grating directly to the camera sensor, with a spacer of around 1 mm. (ii) Polar-CGM enables single-shot measurements of Jones vectors and two-shot measurements of Jones matrices, as is the case for the most advanced techniques. Some studies proposed single-shot measurement of Jones matrices, but at the cost of a high experimental complexity, both on the illumination and detection paths.[19−21,24,25,29] They are also based on strong assumptions that are not always valid. In the context of nanophotonic metrology, the main advantage of the single-shot capability is not necessarily the investigation of rapidly evolving samples, like in biology, but rather the simultaneous acquisition of all polarization channels. This strongly simplifies the measurement procedure and improves the robustness and precision of the measurement, since mechanical drift, vibrations, illumination fluctuations, and static imperfections of the optical system affect all polarization channels equally. While single-shot operation is especially important for dynamic biological systems, in nanophotonics it remains a key asset for accurate, robust, and easily deployable polarization-resolved measurements. (iii) CGM is compatible with broadband and spatially incoherent illumination (LEDs, monochromators), making it easy to conduct spectral studies. Varying the illumination wavelength is complex with techniques that require a laser illumination, such as DHM, or based on metasurfaces that are usually designed only for a specific wavelength,[7,10−12,15,16,28] with a few exceptions.[14] (iv) Unlike DHM that features speckle noise that cannot be damped using image averaging, CGM is a shot-noise limited technique, making it possible to arbitrarily damp the noise amplitude by averaging images. Moreover, even with a single exposure, the noise on CGM images is already on the order of 0.3 nm in wavefront, that is, around $\lambda/1000$, which is particularly low for a QPI technique. This explains why CGM pioneered all the QPI-related applications in nanophotonics and the detection of nano-objects.[50−52,62−64] (v) Polar-CGM requires only the design of a camera-like system, making this approach intrinsically cost-effective, compared to techniques that require a modification of the microscope itself.[5,17,19−21,24−26,28−30] (vi) The price to pay to enrich a

Downloaded from pubs.acs.org/ancac3/article-pdf/20/42/28193/6887767672/acsnano.6c06635.pdf by guest on 06 November 2026

https://doi.org/10.1021/acsnano.6c06635
ACS Nano 2026, 20, 28193−28206

single image acquisition with more than simply the intensity is to lose imaging definition. In CGM or DHM, 3 × 3 camera pixels are needed to build one intensity or phase pixel. In polar-CGM, it becomes 6 × 6, further reducing the final image definition. This reduction in image *definition* is not necessarily accompanied by a loss in image *information*. If the microscope magnification is large enough or the camera pixel size small enough, one can still reach the diffraction limit, if needed (see Section S2.8).

The theory we developed here to extract Jones matrices was illustrated using CGM. However, it applies to any QPI or WI technique. In addition to the applications in nanophotonics presented in this study, polar-CGM could be applied to 2D materials or complex laser beam characterization. Polarization microscopy is also of great current interest in biology, but mostly for fluorescence and Raman imaging.[65,66] The counterpart related to elastic scattering is much less developed.

Because of all the benefits of polar-CGM compared with the existing related techniques, we believe it also represents the ideal metrology tool for the polarization-resolved characterization of a wide variety of biological samples, 2D materials or advanced nanophotonic systems. These possible research directions support the idea that polar-CGM will continue to develop, lead to numerous applications, and have a strong impact across many imaging communities.

METHODS/EXPERIMENTAL SECTION

Polar-CGM Experimental Setup

Polar-CGM measurements were performed on a standard, yet custom-made, transmission microscope equipped with the polarization-resolved QLSI imaging system. Illumination was provided by a grating-based fiber-coupled monochromator coupled to a laser-driven light source (Energetiq; Mountain Photonics GmbH, supplied by Opton Laser International). The monochromator bandwidth was set to approximately 6 nm. Spectroscopic polar-CGM measurements were carried out by tuning the illumination wavelength of the monochromator over the visible range. Circularly polarized illumination was generated using a linear polarizer followed by a tunable waveplate (LCC1423A with KLC101 controller, Thorlabs). For each illumination wavelength, the retardance was adjusted using a clear region of the sample until the four polarization channels of the camera exhibited identical average intensities, corresponding to circular polarization. The opposite handedness was subsequently obtained by rotating the linear polarizer by 90°. The detection system consisted of a polarization camera based on a Sony IMX250MZR/MYR sensor (LUCID Vision Laboratories, 2448 × 2048 pixels, 3.45 μm pixel pitch), integrating linear micropolarizers oriented at 0°, 45°, 90°, and 135° in a 2 × 2 arrangement. A custom QLSI cross-grating with a pitch of 39 μm was fabricated at CEA-Leti (PTA, Grenoble, France). The grating consisted of chromium lines defining transparent square elements with a 0−π checkerboard phase pattern.

The grating was reimaged in front of the camera using a VZM 300 zoom relay lens (Edmund Optics, #39−708), allowing adjustment of both the effective grating-to-camera distance and the transverse magnification. The relay-lens magnification was set to Z = 1.0615, ensuring proper sampling of the QLSI diffraction pattern by the polarization sensor. A grating-to-camera distance of d = 0.80 mm was used for most experiments. Because the effective grating position slightly depends on wavelength owing to the chromaticity of the relay lens, the grating position was adjusted during spectral measurements to maintain a constant effective grating-to-camera distance.

Image Acquisition and Processing

For each experimental condition (wavelength and incident polarization), a reference interferogram was recorded in an empty region of the sample. Then images of the objects were acquired, called interferograms. All the interferograms (objects and references) were processed identically using a custom-made algorithm available on a public repository (https://github.com/baffou/PhaseLAB): Each interferogram was first demosaiced into four subinterferograms corresponding to the 0°, 45°, 90°, and 135° polarization orientations. Each subinterferogram was then processed using the standard QLSI algorithm to retrieve the corresponding intensity and wavefront images. These images were used to reconstruct the Jones vector image using the set-offset-on-clear-area (SOCA) procedure or, when no such region was available, using the quadrature offset correction (QOC) described in the Supporting Information, Section S4. Jones matrices were determined from measurements performed under two orthogonal incident polarization states using the least-squares reconstruction described in Supporting Information, Section S8. The resulting Jones matrices were subsequently used to determine the eigenpolarizations, complex eigen-transmittances, linear birefringence, linear dichroism, and 2D polarizabilities of the metasurfaces.

Sample Fabrication

The plasmonic metasurfaces consisted of square arrays of gold nanorods fabricated by electron-beam lithography. Each array covered an area of 20 × 20 μm^2. The nanorods were 80 nm long, 40 nm wide, and 40 nm thick, and were deposited on a 5 nm-thick titanium adhesion layer. The array periods were 120 and 80 nm along the long and short nanorod axes, respectively. The dielectric metasurfaces consisted of freestanding polymer nanofins fabricated from ma-N 2410 negative-tone resist (Micro Resist Technology GmbH, Germany), following the previously reported fabrication procedure.[61] Each nanofin had dimensions of 400 × 140 × 1700 nm^3. Spatially varying nanofin orientations were used to form the nonuniform vectorial metasurfaces investigated in Figure 6.

Numerical Simulations

The optical response of the gold-nanorod metasurface was simulated using the finite-element method with periodic boundary conditions, using the open-source Gmsh/GetDP finite-element framework.[67] The simulated unit cell measured 120 × 80 nm^2 and contained a single gold nanorod 80 nm long, 40 nm wide, and 40 nm thick, deposited on a 5 nm-thick titanium adhesion layer on a glass substrate. Complex eigen-transmittances and the corresponding 2D polarizabilities were calculated over the 500−800 nm wavelength range and compared with the polar-CGM measurements.

ASSOCIATED CONTENT

Data Availability Statement

Most of the raw data supporting the findings of this study are openly available at 10.5281/zenodo.10888480. All data required to reproduce the results can be obtained from the corresponding author upon reasonable request. The MATLAB codes used in this study are available on the internet, via the PhaseLAB toolbox: https://github.com/baffou/PhaseLAB.

Supporting Information

The Supporting Information is available free of charge at https://pubs.acs.org/doi/10.1021/acsnano.6c06635.

PhaseLAB codes(PDF)

Description of the interferogram demosaicing procedure. Guide to adjusting the polar-CGM setup. Description of the samples. Theory of absolute Full-Stokes imaging. Imaging of the calibration sample. Description of the polarization ellipse. Description of the S_2 test. Derivation of eq 16. Retrieval of complex transmittances and angle values from the estimated Jones matrix. Comments on measurement precision. Theory of Mueller matrix imaging. Discussion on metasurfaces and partially polarized light. Optical properties characterizing a metasurface. Numerical simulations of the optical properties of the metasurface. Origin of the polarization

Downloaded from pubs.acs.org/ancac3/article-pdf/20/42/28193/6887672/acsnano.6c06635.pdf by guest on 06 November 2026

https://doi.org/10.1021/acsnano.6c06635
ACS Nano 2026, 20, 28193−28206

ellipse orientation. Animated figures of the results. Limitations of the cross-grating distance on the metalens image. Convention for circular polarization handedness (PDF)

AUTHOR INFORMATION

Corresponding Author

Guillaume Baffou − *Aix-Marseille University, CNRS, Centrale Med, Institut Fresnel, Marseille 13013, France;* orcid.org/0000-0003-0488-1362; Email: guillaume.baffou@fresnel.fr

Authors

Julien Flamant − *Université de Lorraine, CNRS, CRAN, Nancy F-54000, France*

Baptiste Marthy − *Aix-Marseille University, CNRS, Centrale Med, Institut Fresnel, Marseille 13013, France*

Khosro Zangeneh Kamali − *Department of Physics, Chalmers University of Technology, Gothenburg 412 96, Sweden;* orcid.org/0000-0002-3160-737X

Nathan Ullberg − *Aix-Marseille University, CNRS, Centrale Med, Institut Fresnel, Marseille 13013, France;* orcid.org/0000-0002-7264-7992

Guillaume Demesy − *Aix-Marseille University, CNRS, Centrale Med, Institut Fresnel, Marseille 13013, France*

Patrick Ferrand − *Aix-Marseille University, CNRS, Centrale Med, Institut Fresnel, Marseille 13013, France;* orcid.org/0000-0002-7395-5663

Mikael Käll − *Department of Physics, Chalmers University of Technology, Gothenburg 412 96, Sweden;* orcid.org/0000-0002-1163-0345

Complete contact information is available at: https://pubs.acs.org/10.1021/acsnano.6c06635

Author Contributions

G.B. proposed the idea, built the setup, and developed the image processing algorithms. G.B., B.M. and N.U. conducted the measurements and processed the data. J.F. developed the theory. K.Z.K. and M.K. fabricated the metasurface samples and provided their expertise in metasurface science. P.F. provided his expertise in experimental and theoretical polarimetry. G.D. ran the numerical simulations. All authors discussed the results and contributed to the writing of successive versions of the manuscript.

Funding

This project received funding from the European Research Council (ERC) under the European Union's HORIZON Research and Innovation Programme (proposal number no. 101101026, project MultiPhase). This work was partly supported by the French RENATECH network (CEA Leti, PTA), which fabricated the QLSI grating used in this study.

Notes

The authors declare no competing financial interest.

ACKNOWLEDGMENTS

We thank Myriam Zerrad for lending us a polarization camera during the early stages of this project.

REFERENCES

(1) He, C.; He, H.; Chang, J.; Chen, B.; Ma, H.; Booth, M. J. Polarisation optics for biomedical and clinical applications: a review. *Light Sci. Appl.* **2021**, *10*, 194.

(2) Qi, J.; Elson, D. S. Mueller polarimetric imaging for surgical and diagnostic applications: a review. *J. Biophotonics* **2017**, *10*, 950−982.

(3) Baumann, B. Polarization Sensitive Optical Coherence Tomography: A Review of Technology and Applications. *Appl. Sci.* **2017**, *7*, 474.

(4) Ghosh, N.; Viktin, I. A. Tissue polarimetry: concepts, challenges, applications, and outlook. *J. Biomed. Opt.* **2011**, *16*, 110801.

(5) Colomb, T.; Dahlgren, P.; Beghuin, D.; Cuche, E.; Marquet, P.; Depeursinge, C. Polarization imaging by use of digital holography. *Appl. Opt.* **2002**, *41*, 27−37.

(6) Hsu, W. L.; Myhre, G.; Balakrishnan, K.; Brock, N.; Ibn-Elhaj, M.; Pau, S. Full-Stokes imaging polarimeter using an array of elliptical polarizer. *Opt. Express* **2014**, *22*, 3063−3074.

(7) Arbabi, E.; Kamali, S. M.; Arbabi, A.; Faraon, A. Full-Stokes Imaging Polarimetry Using Dielectric Metasurfaces. *ACS Photonics* **2018**, *5*, 3132−3140.

(8) Ge, B.; Takiguchi, Y.; Yaqoob, Z.; So, P. T. C. Single-Shot Optical Anisotropy Imaging with Quantitative Polarization Interference Microscopy. *Laser Photonics Rev.* **2018**, *12*, 1800070.

(9) Ge, B.; Zhang, Q.; Zhang, R.; Lin, J. T.; Tseng, P. H.; Chang, C. W.; Dong, C. Y.; Zhou, R.; Yaqoob, Z.; Bischofberger, I.; et al. Single-Shot Quantitative Polarization Imaging of Complex Birefringent Structure Dynamics. *ACS Photonics* **2021**, *8*, 3440−3447.

(10) Rubin, N. A.; Chevalier, P.; Juhl, M.; Tamagnone, M.; Chipman, R.; Capasso, F. Imaging polarimetry through metasurface polarization gratings. *Opt. Express* **2022**, *30*, 9389−9412.

(11) Fan, Q.; Xu, W.; Hu, X.; Zhu, W.; Yue, T.; Yan, F.; Lin, P.; Chen, L.; Song, J.; Lezec, H.; Agrawal, A.; Lu, Y.; Xu, T. Disordered metasurface enabled single-shot full-Stokes polarization imaging leveraging weak dichroism. *Nat. Commun.* **2023**, *14*, 7180.

(12) Huang, Z.; Zheng, Y.; Li, J.; Cheng, Y.; Wang, J.; Zhou, Z. K.; Chen, L. High-Resolution Metalens Imaging Polarimetry. *Nano Lett.* **2023**, *23*, 10991−10997.

(13) Cox, M. A.; Rosales-Guzmán, C. Real-time Stokes polarimetry using a polarization camera. *Appl. Opt.* **2023**, *62*, 7828−7836.

(14) Hu, Y.; Jiang, Y.; Zhang, Y.; Wang, Q.; Pan, M.; Duan, H. Achromatic Full Stokes Polarimetry Metasurface for Full-Color Polarization Imaging in the Visible Range. *Nano Lett.* **2024**, *24*, 13018−13026.

(15) Soma, G.; Komatsu, K.; Ren, C.; Nakano, Y.; Tanemura, T. Metasurface-enabled non-orthogonal four-output polarization splitter for non-redundant full-Stokes imaging. *Opt. Express* **2024**, *32*, 34207.

(16) Blochet, B.; Lelu, G.; Alonso, M. A.; Guillon, M. Quantitative polarimetric wavefront imaging. *Optica* **2025**, *12*, 907.

(17) Wang, Z.; Millet, L. J.; Gillette, M. U.; Popescu, G. Jones phase microscopy of transparent and anisotropic samples. *Opt. Lett.* **2008**, *33*, 1270.

(18) Kim, Y.; Jeong, J.; Jang, J.; Kim, M. W.; Park, Y. K. Polarization holographic microscopy for extracting spatio-temporally resolved Jones matrix. *Opt. Express* **2012**, *20*, 9948.

(19) Liu, X.; Wang, B. Y.; Guo, C. S. One-step Jones matrix polarization holography for extraction of spatially resolved Jones matrix of polarization-sensitive materials. *Opt. Lett.* **2014**, *39*, 6170−6173.

(20) Yang, T. D.; Park, K.; Kang, Y. G.; Lee, K. J.; Kim, B. M.; Choi, Y. Single-shot digital holographic microscopy for quantifying a spatially-resolved Jones matrix of biological specimens. *Opt. Express* **2016**, *24*, 29302.

(21) Sreelal, M. M.; Vinu, R. V.; Singh, R. K. Jones matrix microscopy from a single-shot intensity measurement. *Opt. Lett.* **2017**, *42*, 5194−5197.

(22) Baroni, A.; Chamard, V.; Ferrand, P. Extending Quantitative Phase Imaging to Polarization-Sensitive Materials. *Phys. Rev. Appl.* **2020**, *13*, 054028.

(23) Jiao, Y.; Kandel, M. E.; Liu, X.; Lu, W.; Popescu, G. Real-time Jones phase microscopy for studying transparent and birefringent specimens. *Opt. Express* **2020**, *28*, 34190.

Downloaded from pubs.acs.org/ancac3/article-pdf/20/42/28193/6887672/acsnano.6c06635.pdf by guest on 06 November 2026

(24) Park, K.; Yang, T. D.; Seo, D.; Hyeon, M. G.; Kong, T.; Kim, B. M.; Choi, Y.; Choi, W.; Choi, Y. Jones Matrix Microscopy for Living Eukaryotic Cells. *ACS Photonics* **2021**, *8*, 3042−3050.
(25) Chen, G. X.; Zhang, Y. Y.; Yang, Y.; Huang, H. Y.; Yue, Q. Y.; Guo, C. S. Compact common-path polarisation holographic microscope for measuring spatially-resolved Jones matrix parameters of dynamic samples in microfluidics. *Opt. Commun.* **2022**, *503*, 127460.
(26) Rathor, M.; Chaubey, S. K.; Tamang, R.; Koch, B.; Singh, R. K. Single-Shot Quantitative Polarization Imaging of Live Cancer Cells. *ACS Photonics* **2023**, *10*, 3755−3762.
(27) Li, L.; Wang, S.; Zhao, F.; Zhang, Y.; Wen, S.; Chai, H.; Gao, Y.; Wang, W.; Cao, L.; Yang, Y. Single-shot deterministic complex amplitude imaging with a single-layer metalens. *Sci. Adv.* **2024**, *10*, No. eadl0501.
(28) Zaidi, A.; Rubin, N. A.; Meretska, M. L.; Li, L. W.; Dorrah, A. H.; Park, J. S.; Capasso, F. Metasurface-enabled single-shot and complete Mueller matrix imaging. *Nature Photon* **2024**, *18*, 704−715.
(29) Liu, H.; Chen, K.; Liao, D.; Chen, Z.; Pu, J. Real-Time Jones Matrix Synthesis by Compact Polarization Inline Holographic Microscopy. *Laser Photonics Rev.* **2024**, *18*, 2301261.
(30) Li, G.; Chen, X.; Chen, X.; Li, X.; Zhuang, W.; Ma, J.; Song, Z.; Li, B.; Yuan, C. Single-Shot high Bandwidth-Utilization Jones matrix measurement based on Kramers−Kronig holographic multiplexing. *Opt. Laser Technol.* **2025**, *192*, 113915.
(31) Lu, S. Y.; Chipman, R. A. Homogeneous and inhomogeneous Jones matrices. *J. Opt. Soc. Am. A* **1994**, *11*, 766−773.
(32) Shribak, M.; Oldenbourg, R. Techniques for fast and sensitive measurements of two-dimensional birefringence distributions. *Appl. Opt.* **2003**, *42*, 3009.
(33) Mehta, S. B.; Shribak, M.; Oldenbourg, R. Polarized light imaging of birefringence and diattenuation at high resolution and high sensitivity. *J. Opt.* **2013**, *15*, 094007.
(34) Guo, S. M.; Yeh, L. H.; Folkesson, J.; Ivanov, I. E.; Krishnan, A. P.; Keefe, M. G.; Hashemi, E.; Shin, D.; Chhun, B. B.; Cho, N. H.; Leonetti, M. D.; Han, M. H.; Nowakowski, T. J.; Mehta, S. B. Revealing architectural order with quantitative label-free imaging and deep learning. *eLife* **2020**, *9*, No. e55502.
(35) Kim, J.; Song, S.; Kim, H.; Kim, B.; Park, M.; Oh, S. J.; Kim, D.; Cense, B.; Huh, Y. M.; Lee, J. Y.; Joo, C. Ptychographic lens-less birefringence microscopy using a mask-modulated polarization image sensor. *Sci. Rep.* **2023**, *13*, 19263.
(36) Deng, Z. L.; Wang, Z. Q.; Li, F.; Hu, M.; Li, X. Multi-freedom metasurface empowered vectorial holography. *Nanophotonics* **2022**, *11*, 1725−1739.
(37) Jing, W.; Deng, J.; Zhu, T.; Zhang, Y.; Ye, J.; Zhou, J.; Chen, X. Monolithic High-Accuracy Long-Wave Infrared Full-Stokes Polarimeter Based on a Meta-QWIP. *Laser Photonics Rev.* **2026**, *20*, No. e01411.
(38) Tahmi, Y.; Ansquer, M.; Coulon, P.-M.; Chenot, S.; Brändli, V.; Majorel, C.; Patoux, A.; Colom, R.; Wattellier, B.; Genevet, P.; Khadir, S. Phase Characterization of Singular Metasurfaces. *ACS Photonics* **2025**, *12*, 6081−6090.
(39) Chaumet, P. C.; Bon, P.; Maire, G.; Sentenac, A.; Baffou, G. Quantitative phase microscopies: accuracy comparison. *Light Sci. Appl.* **2024**, *13*, 288.
(40) Song, Q.; Liu, X.; Qiu, C.-W.; Genevet, P. Vectorial metasurface holography. *Appl. Phys. Rev.* **2022**, *9*, 011311.
(41) Tahara, T.; Shimobaba, T.; Kozawa, Y. Review on imaging and sensing with holography. *J. Opt.* **2025**, *27*, 043005.
(42) Nguyen, T. L.; Pradeep, S.; Judson-Torres, R. L.; Reed, J.; Teitell, M. A.; Zangle, T. A. Quantitative Phase Imaging: Recent Advances and Expanding Potential in Biomedicine. *ACS Nano* **2022**, *16*, 11516−11544.
(43) Park, Y. K.; Depeursinge, C.; Popescu, G. Quantitative phase imaging in biomedicine. *Nat. Photonics* **2018**, *12*, 578−589.
(44) Lui, Y.; Uttam, S. Perspective on quantitative phase imaging to improve precision cancer medicine. *J. Biomed. Opt.* **2024**, *29*, S22705.
(45) Cacace, T.; Bianco, V.; Ferraro, P. Quantitative phase imaging trends in biomedical applications. *Opt. Lasers Eng.* **2020**, *135*, 106188.
(46) Baffou, G. Wavefront microscopy using quadriwave lateral shearing interferometry: from bioimaging to nanophotonics. *ACS Photonics* **2023**, *10*, 322−339.
(47) García Rodríguez, B.; Olsén, E.; Skärberg, F.; Volpe, G.; Höök, F.; Midtvedt, D. S. Optical label-free microscopy characterization of dielectric nanoparticles. *Nanoscale* **2025**, *17*, 8336−8362.
(48) Priscilla, N.; Sulejman, S. B.; Roberts, A.; Wesemann, L. New Avenues for Phase Imaging: Optical Metasurfaces. *ACS Photonics* **2024**, *11*, 2843−2859.
(49) Kossowski, N.; Tahmi, Y.; Loucif, A.; Lepers, M.; Wattellier, B.; Vienne, G.; Khadir, S.; Genevet, P. Metrology of metasurfaces: optical properties. *npj Nanophotonics* **2025**, *2*, 5.
(50) Khadir, S.; Andrén, D.; Chaumet, P. C.; Monneret, S.; Bonod, N.; Käll, M.; Sentenac, A.; Baffou, G. Full optical characterization of single nanoparticles using quantitative phase imaging. *Optica* **2020**, *7*, 243−248.
(51) Khadir, S.; Bon, P.; Vignaud, D.; Galopin, E.; McEvoy, N.; McCloskey, D.; Monneret, S.; Baffou, G. Optical Imaging and Characterization of Graphene and Other 2D Materials Using Quantitative Phase Microscopy. *ACS Photonics* **2017**, *4*, 3130−3139.
(52) Khadir, S.; Andrén, D.; Verre, R.; Song, Q.; Monneret, S.; Genevet, P.; Käll, M.; Baffou, G. Metasurface optical characterization using quadriwave lateral shearing interferometry. *ACS Photonics* **2021**, *8*, 603−613.
(53) Primot, J.; Guérineau, N. Extended Hartmann Test Based on the Pseudoguiding Property of a Hartmann Mask Completed by a Phase Chessboard. *Appl. Opt.* **2000**, *39*, 5715−5720.
(54) Primot, J.; Guérineau, N. Achromatic optical interferometer with continuously adjustable sensitivity. U.S. Patent 6,577,403 B1, 2000.
(55) Baffou, G. Quantitative phase microscopy using quadriwave lateral shearing interferometry (QLSI): principle, terminology, algorithm and grating shadow description. *J. Phys. D: Appl. Phys.* **2021**, *54*, 294002.
(56) Bon, P.; Maucort, G.; Wattellier, B.; Monneret, S. Quadriwave lateral shearing interferometry for quantitative phase microscopy of living cells. *Opt. Express* **2009**, *17*, 13080−13094.
(57) Marthy, B.; Bénéfice, M.; Baffou, G. Single-shot quantitative phase-fluorescence imaging using cross-grating wavefront microscopy. *Sci. Reports* **2024**, *14*, 2142.
(58) Marthy, B.; Baffou, G. Cross-grating phase microscopy (CGM): In silico experiment (insilex) algorithm, noise and accuracy. *Opt. Commun.* **2022**, *521*, 128577.
(59) Genevet, P.; Capasso, F.; Aieta, F.; Khorasaninejad, M.; Devlin, R. Recent advances in planar optics: from plasmonic to dielectric metasurfaces. *Optica* **2017**, *4*, 139−152.
(60) Baffou, G. Baffou/PhaseLAB, 2026. https://github.com/baffou/PhaseLAB, accessed Sept, 2026.
(61) Andrén, D.; Martínez-Llinas, J.; Tassin, P.; Käll, M.; Verre, R. Large-Scale metasurface made by an exposed resist. *ACS Photonics* **2020**, *7*, 885−892.
(62) Bon, P.; Linarès-Loyez, J.; Feyeux, M.; Alessandri, K.; Lounis, B.; Nassoy, P.; Cognet, L. Self-interference 3D super-resolution microscopy for deep tissue investigations. *Nat. Methods* **2018**, *15*, 449−454.
(63) Linarès-Loyez, J.; Ferreira, J. S.; Rossier, O.; Lounis, B.; Giannone, G.; Groc, L.; Cognet, L.; Bon, P. Self-interference (SELFI) Microscopy for Live Super-Resolution Imaging and Single Particle Tracking in 3D. *Front. Phys.* **2019**, *7*, 68.
(64) Nguyen, M. C.; Bonnaud, P.; Dibsy, R.; Maucort, G.; Lyonnais, S.; Muriaux, D.; Bon, P. Label-free single nanoparticle identification and characterization including infectious emergent virus. *Small* **2024**, *20*, 2304564.
(65) Brasselet, S.; Alonso, M. A. Polarization microscopy: from ensemble structural imaging to single-molecule 3D orientation and localization microscopy. *Optica* **2023**, *10*, 1486−1510.
(66) Er, E.; Chow, T. H.; Liz-Marzán, L. M.; Kotov, N. A. Circular Polarization-Resolved Raman Optical Activity: A Perspective on

Downloaded from pubs.acs.org/ancac3/article-pdf/20/42/28193/6887672/acsnano.6c06635.pdf by guest on 06 November 2026

Chiral Spectroscopies of Vibrational States. *ACS Nano* **2024**, *18*, 12589−12597.
(67) Demésy, G.; Zolla, F.; Nicolet, A.; Commandré, M. All-purpose finite element formulation for arbitrarily shaped crossed-gratings embedded in a multilayered stack. *J. Opt. Soc. Am. A* **2010**, *27*, 878−889.

Downloaded from pubs.acs.org/ancac3/article-pdf/20/42/28193/6887672/acsnano.6c06635.pdf by guest on 06 November 2026

https://doi.org/10.1021/acsnano.6c06635
ACS Nano 2026, 20, 28193−28206